Mechanisms of surface and volume light scattering from *Caenorhabditis elegans* revealed by angle-resolved measurements

Zihao (John) Li and Christopher Fang-Yen*

Department of Biomedical Engineering, College of Engineering, The Ohio State University, Columbus, OH 43210, USA

*Correspondence should be addressed to C.F.-Y. (fang-yen.1@osu.edu)

Abstract

The roundworm *Caenorhabditis elegans* has become a widely studied model system in biology in part due to its small size and optical accessibility. Optical imaging of *C. elegans* primarily relies on scattering of light to generate contrast between the animal and its surroundings, and/or contrast to resolve internal structures within the body. However, the mechanisms of light scattering by *C. elegans*, and how they influence image contrast, are not well understood, and optimization of contrast is typically performed in a trial-and-error fashion. To address this gap, we performed measurements of light scattering from *C. elegans* on laboratory substrates under varied illumination angles, wavelength, substrate material, bacterial seeding, and index matching conditions. By combining these results with those of computational simulations, we find that light scattering arises via two components that exhibit distinct angular and spatial distributions: volume scattering within the body and surface scattering at the boundaries between the worm and its surroundings. We elucidated how volume and surface scattering interact with each other and collectively contribute to the overall scattering. Informed by these findings, we determined the illumination angle range, wavelength

range, and substrate material that optimize imaging contrast. Our findings provide practical strategies for optimizing image quality across a range of imaging systems.

Introduction

The microscopic nematode *C. elegans* is one of the most widely studied model organisms in biology due to its short life cycle, genetic accessibility, and compact anatomy [1, 2]. Its optical accessibility, fully mapped connectome [3], and rich repertoire of behaviors [4] have made it a valuable system for *in vivo* imaging of neural activity [5-7], behavioral dynamics [8-10], and genetic perturbations [10, 11]. Recent advances in automation [11-16] have enabled high-throughput genetic and pharmacological screening using *C. elegans*.

One of the strengths of *C. elegans* is its amenability to optical imaging. Many assays of behavior, morphology, aging, and development rely on obtaining images of worms with high contrast relative to their surroundings [17-21]. Since like most biological tissues, *C. elegans* exhibits relatively low optical absorption over optical wavelengths, most of the optical contrast is provided by scattering, i.e. changes in direction of incident light rays [22].

In any imaging system, lenses or other optical elements are configured to focus light collected from a certain range of angles. Two imaging modes can be differentiated by whether the illumination angles are within the range of collection by the optical system [23, 24]. In a bright field imaging configuration, the illumination rays are within the collection angle of the optics. Optical scattering by the object diverts some of the light away from the collection angles, causing the object to appear darker than its surroundings. By contrast, in a dark field imaging configuration, the illumination light is outside the collection angle of the optical system;

scattering by the object causes some of this light to be collected, and the object appears bright against a dark background.

The amount and angular distribution of light scattering are highly sensitive to illumination angle, wavelength, and the optical properties of the object and background medium. In practice, many imaging systems rely on empirically chosen parameters, without a systematic understanding of how these variables affect image contrast.

Light scattering in biological tissues has previously been studied primarily in the context of biomedical imaging [22, 25]. Prior theoretical descriptions of light scattering in biological tissues include those applying Mie theory [26, 27] which describes scattering from spheres as a function of diameter and refractive index, and the Henyey–Greenstein phase function [28, 29], which describes the degree of anisotropy occurring during scattering. Angle-dependent scattering profiles have been characterized for tissue sections [30-32], tissue-mimicking phantoms [33], and single cells [32, 34]. However, to our knowledge light scattering from intact, living, multicellular organisms such as *C. elegans* has not been examined in detail.

In this study, we developed and applied methods for angle-resolved measurements of light scattering from *C. elegans*. Supported by experimental observations and computational modeling, we find that light scattering from *C. elegans* arises from a combination of volume scattering within the animal body and surface scattering due to the refractive index mismatch at the interface between the worm and its surroundings. We probe the interaction between the volume and surface scattering and reveal how together they shape the overall scattering. Based on these findings, we determined optimal values for several experimental parameters including illumination angle, illumination wavelength, and substrate material that maximize optical contrast.

Our work provides a quantitative framework for understanding light scattering in *C. elegans* and offers practical guidance for optimizing image quality. Moreover, the physical principles outlined here will inform optimization strategies for imaging other organisms.

Results

Angle-resolved scattering functions

To quantitatively describe light scattering from *C. elegans*, we illuminated worms on agar plates at specific angles using a ring of light-emitting diodes (LEDs) and captured images using a camera and lens (Fig. 1A, Material and Methods). We imaged worms against a background of either agar seeded with food bacteria or bare (unseeded) agar (Fig. 1B). Under illumination at variable angles, the animals exhibit distinct spatially inhomogeneous scattering patterns (Fig. 1B). The contrast of the animal against its background also changes with θ (Fig. 1B).

We aimed to quantitatively describe the observed angle-dependent optical scattering and image contrast. Using the images recorded with different illumination angles, we calculated the scattering function p(θ), which has units of sr^{-1} (inverse steradian) and describes the probability per solid angle of a photon scattering by a polar angle θ relative to its original trajectory (Fig. 1A) [35, 36]. The value of the scattering function at θ = 0º represents the probability of a ray to be transmitted without scattering.

We measured scattering functions under red light illumination (peak wavelength 629 nm) for *C. elegans,* agar, and bacteria-coated (seeded) agar (Fig. 1C). For both *C. elegans* and agar backgrounds the scattering function is highest at θ = 0º, decreases from 0º to 60º, is roughly constant between 60º and 140º and increases modestly between 140º and 180º.

To determine the effect of scattering angle on image contrast, we defined a contrast index equal to the difference in irradiance between worm and background, both measured at the camera, divided by the sum of irradiance of the worm and background (see Material and Methods). We calculated the contrast index as a function of θ (Fig. 1D). For θ = 0º, the contrast indices are negative (approximately -0.85) for worms on both seeded and unseeded agar plates. This is because at θ = 0º, the system is in the bright field regime, in which the worm appears darker than its surroundings.

For θ > 0º, in the dark field imaging regime, the scattering function for the background decays with angle at a faster rate than that of the worm (Fig. 1C), causing the contrast indices to increase sharply with θ and reach maximum of about 0.65 for θ around 15º (Fig. 1D). For θ > 15º, the contrast indices decrease with θ and reach minimum between 60º and 90º. For θ close to 180º, the image contrast slightly rises for worms on unseeded plates, and we observe a negative contrast index for worms on seeded plates (Fig. 1D).

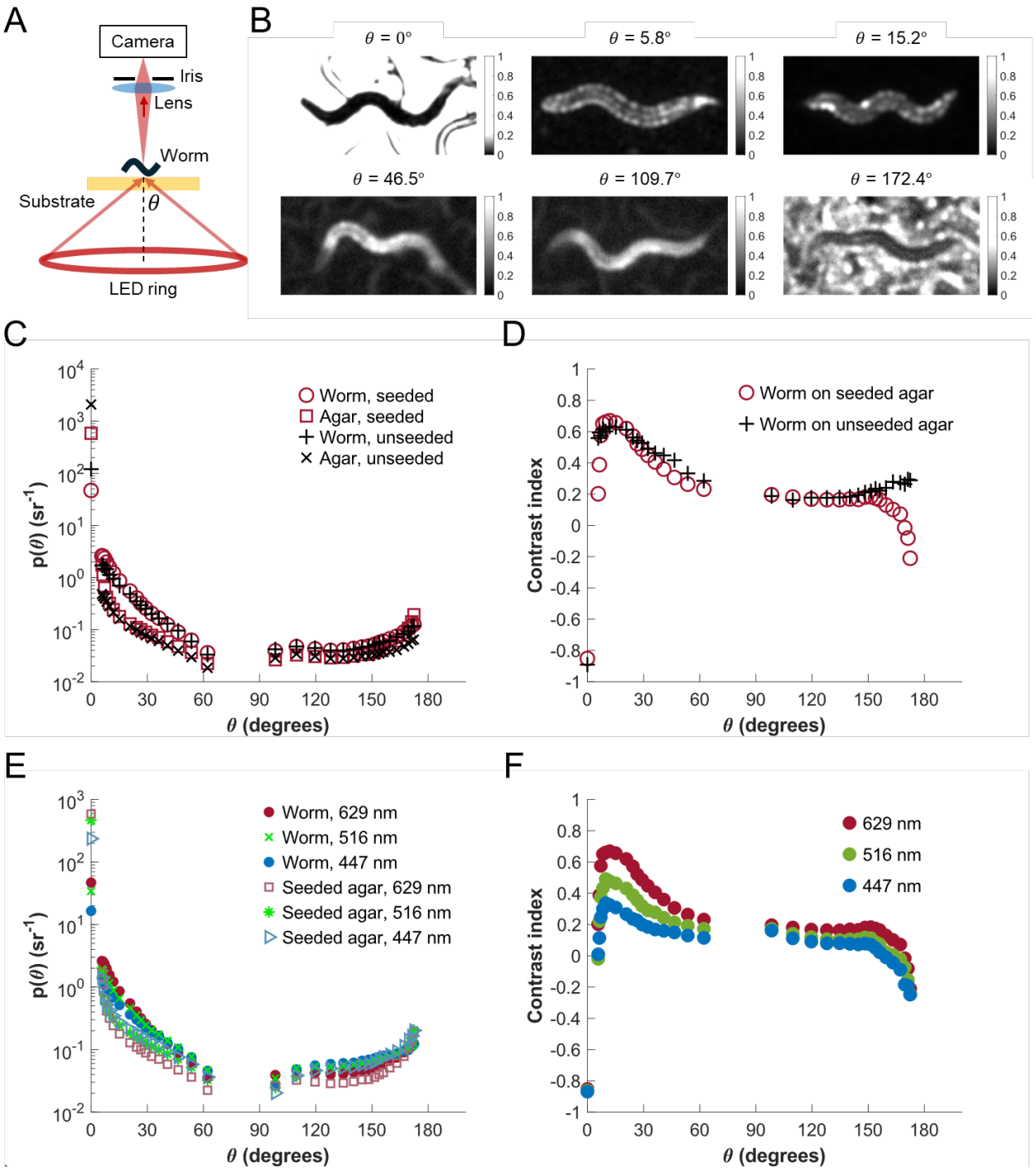

Fig. 1. Angle-resolved, wavelength-dependent scattering functions and image contrast for *C. elegans* on agar substrate. (A) Experimental setup. (B) Representative images of worms and background at different illumination angles (FOV: 1.11 × 0.56 mm). (C) Scattering functions for *C. elegans* on seeded and unseeded agar substrate under red light illumination.

(D) Image contrast as a function of illumination angle θ for *C. elegans* on seeded and unseeded agar plate under red light illumination. (E) Scattering functions for *C. elegans* on seeded agar plates under red, green, and blue light illumination. (F) Image contrast index for *C. elegans* on seeded agar as a function of illumination angle and wavelength.

Wavelength dependence of scattering functions

Optical scattering from biological tissue typically has a strong wavelength dependence [37, 38]. We asked how scattering from *C. elegans* varies with wavelength. We measured the angle-resolved scattering functions for *C. elegans* on seeded agar plates under red (peak wavelength 629 nm), green (516 nm), and blue (447 nm) LED illumination (Fig. 1E). The scattering functions for green and blue light show similar overall shapes as that of red light. We found that light scattering with longer-wavelength illumination is higher for worms but lower for seeded agar, which results in a higher image contrast for red illumination than for green or blue (Fig. 1F). The maximum contrast index for red illumination (approximately 0.7) is about twice than of blue (approximately 0.35). For θ between 90º to 180º, scattering functions with longer wavelengths are lower for both worms and seeded agar and the contrast indices for red are higher than green and blue. For all three wavelengths, we observe negative contrast when θ is near 180º. These results suggest that red illumination is better than green or blue in terms of generating contrast in images.

Our results show that the scattering functions near θ = 0º are higher for longer wavelength for both *C. elegans* and seeded agar. It indicates that the proportion of the light that is forward transmitted without scattering increases with wavelength, consistent with results from prior studies that the optical reduced scattering coefficient (μ_s') generally decreases with wavelength [37].

Empirical analysis of volume and surface scattering

We sought to understand the mechanisms contributing to the observed angle-dependent scattering functions from *C. elegans*. We reasoned that light scattering from *C. elegans* could arise from two sources: (1) volume scattering within the animal body due to refractive index variations and (2) surface scattering from refractive index mismatch at the boundaries between the worm and the air and/or the substrate (Fig. 2A).

To help distinguish between these two types of scattering, we first isolated the volume scattering by minimizing the surface scattering via approximate refractive index matching. Most biological tissues have an index of refraction slightly higher than that of water [39]. The *C. elegans* cuticle has been measured to have a refractive index about $n = 1.35\text{-}1.37$, only slightly higher than that of water [40]. To achieve approximate index matching, we placed a gelatin pad ($n \approx 1.36$) on the agar plate in order to eliminate the worm-to-air interface and surround the animals with media with similar refractive index to that of the worm (Fig. 2B). After index matching, the observed scattering function should be almost entirely due to volume scattering.

Fig. 2C depicts the scattering functions for *C. elegans* and bacteria-seeded agar in the index-matching experiment. For $\theta = 0^\circ$, scattering functions for the index-matched case are higher than for the non-index-matched case for both worm and background, implying that index matching increases the forward transmission. For $\theta > 0^\circ$, index matching caused the scattering function to decrease. For the background, scattering function for the index-matched case is lower than for non-index matching for θ near 0° and 180°, and slightly higher elsewhere.

We calculated the contrast indices due to volume scattering from the worm and background (Fig. 2D). For $\theta = 0^\circ$, in the bright field imaging regime, the image contrast for index matching is similar to non-index matching. For $\theta > 0^\circ$, in the dark field imaging regime, the

image contrast reaches maximum around ~10º for index matching and decreases with θ. In general, index matching reduces image contrast (Fig. 2D), implying that the surface scattering helps improving the image contrast.

As in the non-index matched case, we observed that volume scattering in *C. elegans* is dependent on illumination wavelength and red light generates higher image contrast than green or blue (Fig. S1). Our results show that optimal image contrast can be obtained by applying red illumination with an angle of 10º-15º relative to the optical axis. These findings inform useful guidelines for optimizing image quality for *C. elegans* in liquid-based assays [19, 41, 42] or other index-matched environments.

Mechanisms of volume and surface scattering

The experimental observations of optical scattering in the non-index matched and index matched scenarios pose several questions. What mechanisms contribute to the angular dependence of the optical scattering from *C. elegans* and how does it shape the nonlinear change of the image contrast (Fig. 2C and D)? What is the interplay between the volume and the surface scattering and how do they contribute to the overall scattering? Why does the optical scattering exhibit spatially inhomogeneous patterns across the worm's body, sometimes appearing to highlight the outline of the animal (Fig. 1B)?

To explore the mechanisms underlying the angle-dependent scattering, we created a simple computational model of the worm and its surroundings (Fig. 2A). We modeled the adult *C. elegans* as a cylinder (diameter = 50 μm, length = 1000 μm, n = 1.33) on the surface of a rectangular cuboid (n = 1.33) representing the substrate and a concave shaped film (n = 1.33) formed at the either side (Fig. 2A and Fig. S2) representing the capillary water film that forms near the points of contact between the worm and the agar substrate [43]. We set the volume

scattering within the cylinder to follow the Henyey-Greenstein phase function [28], widely used to model light scattering within biological tissues [29], with anisotropy parameter g equal to 0.83 and scattering mean free path 12 μm (optimization of free parameters is described in Materials and Methods). To simulate the index matched case, we eliminated the worm-to-air interface by adding a medium (n = 1.33) representing the index matching pad (Fig. 2B).

Using these models, we simulated scattering functions for both the index matched and non-index matched cases. We observed that the simulated scattering functions show good consistency with the experimental observations for both the index matched and non-index matched cases (Fig. 2E). Our computational models successfully capture important features of experimental data. For θ = 0º, scattering functions for index matching is higher than non-index matching. For θ > 0º, the scattering functions decrease with θ, and scattering for index matching is lower than non-index matching. These findings suggest that the presence of surface scattering increases the overall scattering (θ > 0º). Both scattering functions increase for large θ, between 140º and 180º. The back scattering detected at θ = 180º is due to Fresnel reflection (optical reflection occurring at interfaces between media of different refractive indices) (Fig. 2A and B) [44]. The flat horizontal upper surface of the index-matching medium (Fig. 2B) creates a Fresnel reflection for the index matched scenario that is much stronger than that of the non-index matched case.

In addition to calculating the scattering due to volume scattering only (via index matching), we calculated the scattering due to surface scattering alone (by removing volume scattering), the sum of the volume only and surface scattering only models, and finally the scattering in the complete model incorporating both volume and surface scattering (Fig. 2F).

In the surface scattering only model, the worm and water film act as an approximately cylindrical lens. Due to the resulting lensing effect, the surface scattering is strong for θ between 0º and 50º and reaches a minimum around 90º. Next, it increases between 90º and

180º, due to Fresnel reflections occurring at the worm-to-air interface. In comparison, the volume scattering alone exhibits a more uniform angular distribution, gradually decreasing with scattering angle except for peaks near at 0º and 180º due to transmission and Fresnel reflections, respectively.

By comparing the sum of the volume only and surface scattering only models with the complete model incorporating both volume and surface scattering, we can assess the degree of interaction between volume and surface scattering. If volume and surface scattering occur independently, we would expect the sum of the volume only and surface scattering only to equal the complete model. This is indeed the case for large angles, from about 60º to 150º (Fig. 2F) because Fresnel reflection from the upper worm surface is independent of volume scattering occurring inside the animal. However, for angles less than 60º the complete scattering is much smaller than the sum of the surface and volume scattering models. This is because rays coming from below the worm must first go through volume scattering in the worm's body and then surface scattering before being collected by the detector. In this case, the incident ray directions are largely randomized by the volume scattering, causing most of them to scatter into larger angles. On the other hand, the lensing effect of surface scattering in the complete model helps refracting the rays to reach the detector, causing the complete scattering to be somewhat higher than that of pure volume scattering (Fig. 2F).

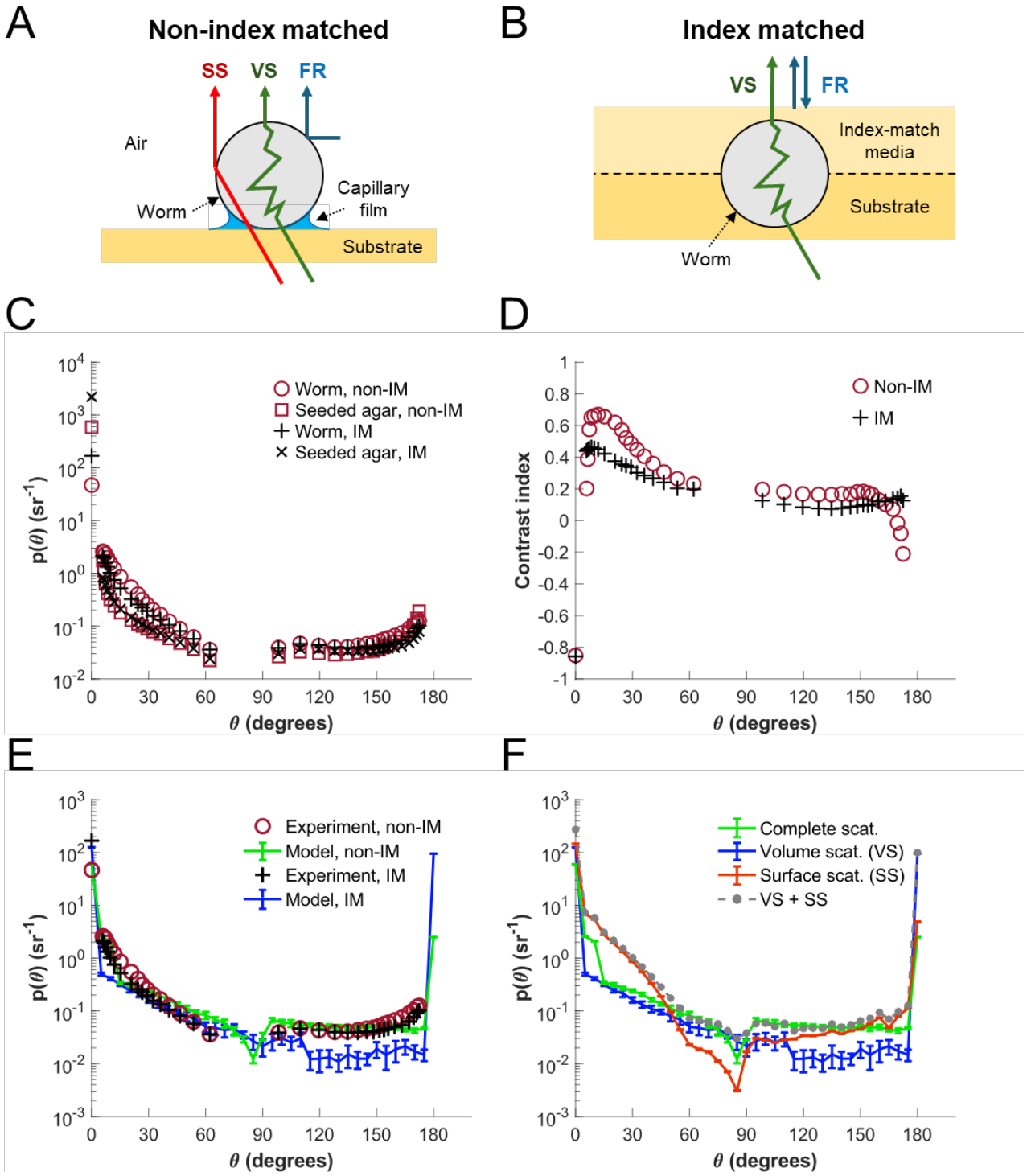

Fig. 2. Analysis of volume and surface scattering from *C. elegans*. (A) Schematic diagram of light scattering from *C. elegans* on a moist substrate. SS: surface scattering; VS: volume scattering; FR: Fresnel reflection. (B) Schematic diagram of light scattering from *C. elegans* on

227 the substrate underneath an index-matching media. (C) Angle-resolved scattering functions for
228 *C. elegans* and seeded agar for non-index matched (non-IM) and index matched (IM) cases. (D)
229 Angle-resolved image contrast of *C. elegans* on seeded agar for non-IM and IM cases. (E)
230 Simulated angle-resolved scattering functions obtained from the computational model for non-
231 IM and IM cases, overlaid with the experimental results. (F) The simulated scattering functions
232 for the volume scattering only, the surface scattering only, the sum of the volume and surface
233 scattering, and the complete scattering.

234

235 Spatial distribution of light scattering

236 We asked how the volume and surface scattering contribute to the spatially
237 inhomogeneous patterns observed in the worm images as a function of angle (Fig. 1B). First,
238 we measured the cross-sectional scattering profile for the animal at various illumination angles
239 (Fig. 3A-D). We noticed that in some images the worm appeared brightest along its edges,
240 whereas in others it appeared brightest at its center. To quantify how much the light scattering
241 is spatially located around the edges of the worm body compared to the center, we defined the
242 edge-to-middle contrast index (EMCI) (see Materials and methods). The EMCI has a range from
243 -1 to 1 with positive EMCI indicating the scattering is brighter around the edges than in the
244 middle. We measured EMCI as a function of θ for the index matched and non-index matched
245 cases (Fig. 3E and F).

246 In the non-index matched case, for $\theta < 10^{\circ}$, stronger scattering is experimentally
247 observed around the edges and weaker in the middle, yielding positive EMCI (Fig. 3E). For $\theta >$
248 10°, scattering is weaker around the edges and stronger in the middle, yielding negative EMCI.
249 When θ approaches 180°, the EMCI turns positive again. In contrast, the EMCI for index-
250 matching is negative for all the experimentally tested θ except for 0° (Fig. 3F). These results

251 indicate that high scattering observed around the edges for θ close to 0º and 180º for the non-
252 index matched scenario are due to the surface scattering. In comparison, the volume scattering
253 consistently concentrates around the middle of the animal body with different θ.

254 Next, we ask whether the observed spatial distribution of scattering can be reproduced
255 by our computational model depicted in Fig. 2A and B. The profiles of scattering across the
256 simulated worm for the representative θ in the scenarios of non-index matching and index
257 matching are shown in Fig. 3B and D, respectively. The simulated EMCIs as functions of θ for
258 both scenarios are respectively shown in Fig. 3E and F. The results from our simulation show
259 high consistency with the experimental data, further supporting the validity of our computational
260 model.

261 Combining the results from Fig. 2F, we can describe the mechanisms underlying the
262 angle-dependent spatial distribution of the scattering. For θ = 0º, in the bright field imaging
263 regime, the light incident to the animal is scattered out of the collection angle of the camera (Fig.
264 1A), causing the animal to appear darker than the background (Fig. 1B, Fig. 3A-D), yielding
265 negative image contrast (Fig. 1D and Fig. 2D) and positive EMCI (Fig. 3E and F). In the dark
266 field imaging regime, for small θ > 0º, the surface scattering is dominant and contributes to the
267 brightened boundaries of the animal due to the lensing effect, yielding positive EMCI (Fig. 3B
268 and E). For larger scattering angles, the volume scattering is dominant, and the scattering
269 spatially distributes around the center, yielding negative EMCI (Fig. 3E and F). The negative
270 contrast index and the positive EMCI observed near θ = 180º for worm on bacteria-seeded agar
271 (Fig. 1B, D, F, Fig. 3A, B, and E) is due to the Fresnel reflection from the substrate.

272 These findings hold important implications for choosing optimal illumination angles for
273 different purposes. For some applications where identification and tracking the animals are
274 more important, smaller angles would be preferable since the surface scattering highlights the
275 object boundaries and overall contrast is highest. For cases in which resolving the internal

structures of *C. elegans* is more important, the illumination should be set to higher angles where the volume scattering is dominant.

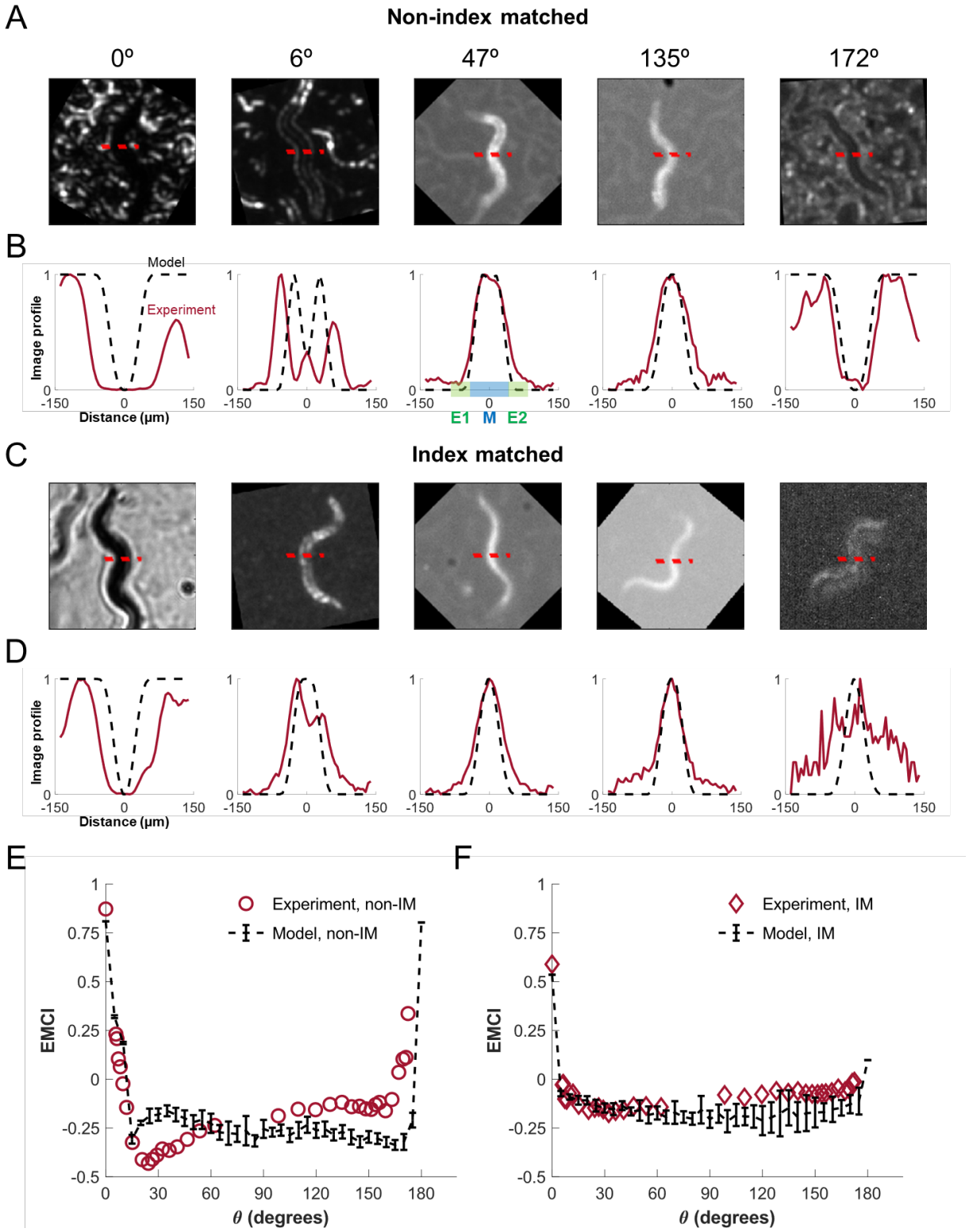

Fig. 3. Spatial distribution of light scattering from *C. elegans*. (A) Images recorded at representative angles for *C. elegans* on seeded agar, without an index matching media (FOV = 1.11 × 1.11 mm). The red dashed line highlights the pixels used for calculating the cross-sectional scattering profiles at the midpoint of the animal. (B) Scattering profiles across the animal body at the representative angles for the non-index matched case. E1, M, and E2 represent the first edge portion, the middle portion, and the second edge portion of the profile used for calculating EMCI. (C) Images recorded at representative angles for *C. elegans* on seeded agar underneath an index matching media. (D) Scattering profiles across the animal body at the representative angles for the index matched case. (E) Experimental and simulated EMCIs as functions of θ for the non-index matched (non-IM) scenario. (F) Experimental and simulated EMCIs as functions of θ for the index matched (IM) scenario.

Optimal illumination for microscopy

To illustrate the consequences of our findings about mechanisms of volume and surface scattering for microscopy of *C. elegans*, we acquired images of worms using imaging systems with higher magnification and numerical aperture (Materials and methods), under various angles of illumination (Fig. 4).

In bright field microscopy (Fig. 4A), the angular range of illumination θ is smaller than that collected by the objective lens. Some of the light incident on the worm scatters out of the collection angles, causing the worm to appear darker than its background. When θ is small, the light collected from the animal is dominated by low-angle scattering (Fig. 4A), which is largely contributed by surface scattering (Fig. 2F). The surface scattering helps improve the contrast of the edges with a tradeoff of lower resolution for the internal structures (Fig. 4B), consistent with the results from our spatial analysis (Fig. 3A, B, and E). To better visualize internal features, the

angular range of illumination should be larger so that more light scattered to high angles due to volume scattering can be collected (Fig. 4C). Compared to an image using narrow angle illumination (Fig. 4B), wider-angle illumination better resolves internal structures within the body, such as pharynx, intestine, and embryos (Fig. 4C).

In dark field microscopy (Fig. 4D), the illumination is outside the acceptance angle of the objective lens. Optical scattering diverts some of the light into the acceptance angle, and the worm appears bright against a dark background (Fig. 4E-F). When the illumination angle is low, more low-angle scattering (surface scattering) is collected, contributing to bright edges and high contrast against the background (Fig. 3A, B, E, and Fig. 4E). In contrast, larger θ causes more high-angle scattering (volume scattering) to be collected, which facilitates the visualization of internal structures (Fig. 4F). Compared to Fig. 4E, higher-angle illumination helps resolving the internal organs (Fig. 4F and G).

For both bright field and dark field imaging, it is important for the illumination angles to be either inside or outside of the lens' acceptance range, but not both simultaneously. Illuminating with a range of angles both inside or outside of the lens' acceptance range results a combination of bright field and dark field images, resulting in low image contrast (Fig. 4H).

These results show that the illumination for microscopy needs to be optimized according to the goals of the study. Low-angle illumination highlights the boundaries and improves the image contrast, which is beneficial for animal tracking and the identification of small independent objects, such as embryos and larvae. By comparison, high-angle illumination helps resolve internal structures, if needed.

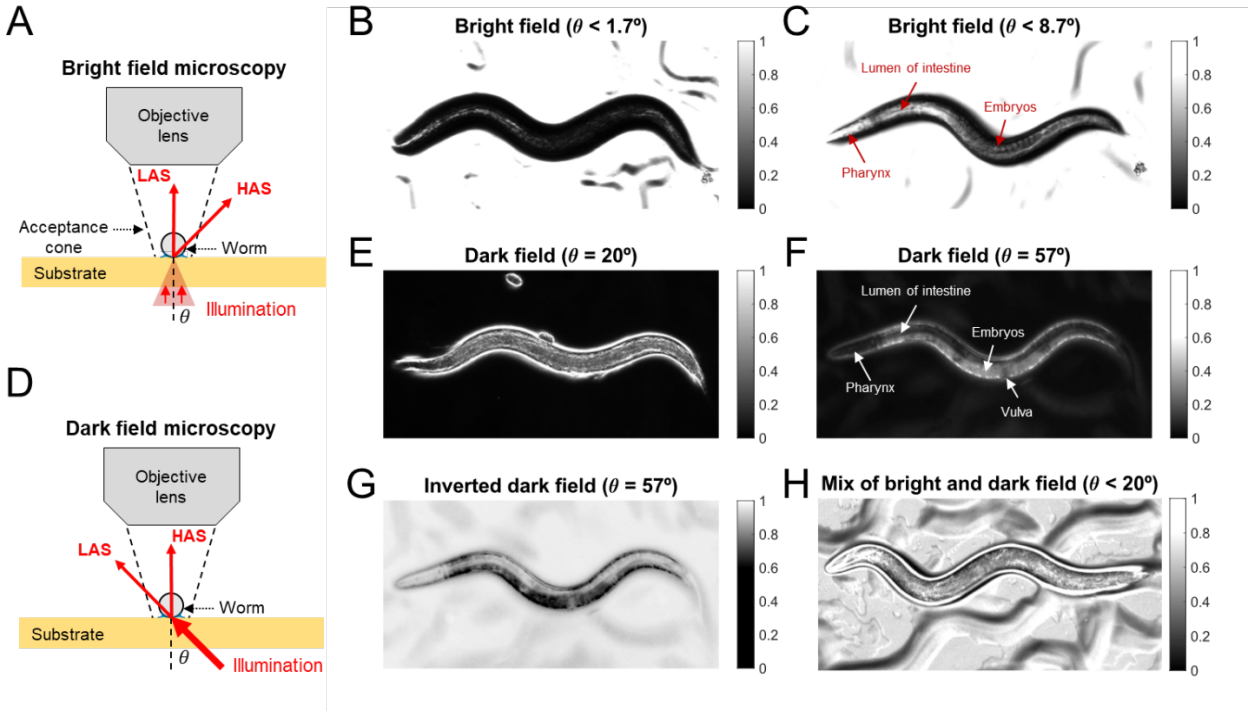

Fig. 4. Effects of illumination angle on bright field and dark field microscopy. (A) Schematic diagram of bright field microscopy. LAS: low-angle scattering; HAS: high-angle scattering. (B) A bright field image of *C. elegans* under narrow-angle illumination (θ < 1.7º) FOV: 1.0 x 0.5 mm. (C) A bright field image of *C. elegans* under wider-angle illumination (θ < 8.7º). (D) Schematic diagram of dark field microscopy. (E) A dark field image of *C. elegans* under low-angle illumination (θ = 20º). (F) A dark field image of *C. elegans* under higher-angle illumination (θ = 57º). (G) Computationally inverted version of F yields an image similar to bright field illumination. (H) A combination of bright field and dark field images of *C. elegans* under illumination applied both inside and outside of the collection angle range of the objective lens (θ < 20º).

Substrate-dependent image contrast

Image contrast is often limited by the amount of scattering in the substrate background. While *C. elegans* is commonly cultured on agar media, other gelling agents may also be used instead of agar [9, 45, 46]. We asked how the composition of the substrate might affect image contrast. We prepared three substrates including agar, gelatin, and gellan gum (Materials and methods), at concentrations that yielded similar gel strengths, and measured scattering functions and image contrast for animals on these substrates (Fig. 5).

Our results show that the scattering functions for all three substrates decrease with θ but show different magnitudes (Fig. 5A). Overall scattering from gelatin and gellan gum is smaller than from agar. This results in the highest image contrast for animals on gelatin and gellan gum, and lowest on agar (Fig. 5B).

We observed that the scattering functions for all the substrates are dependent on illumination wavelength (Fig. S3) and longer-wavelength illumination generates higher image contrast (Fig. 5B, Fig. S3).

We also notice that the imprint due to animal's movement causes significant scattering on gellan gum for $\theta < 10^{o}$ (Fig. S3F), which leads to reduced image contrast (Fig. 5B, Fig. S3F). These imprints may not be favorable for animal identification or tracking but could be helpful for studying locomotion trajectories.

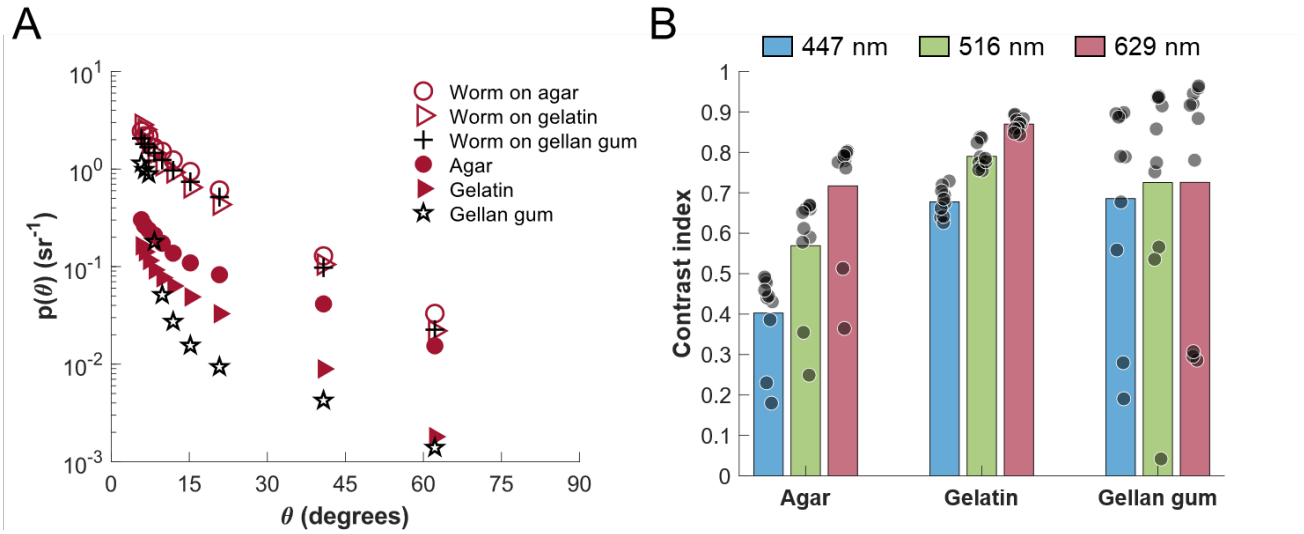

Fig. 5. Scattering functions and image contrast for different substrate polymers. (A) Angle-resolved scattering functions for *C. elegans* on unseeded media made with agar, gelatin, and gellan gum, under red illumination. (B) Image contrast for *C. elegans* on unseeded agar, gelatin, and gellan gum under red, green, and blue illumination. Each dot represents a measurement at an individual illumination angle.

Discussion

In this work, we investigated the mechanisms of light scattering from the nematode *C. elegans* using angle-resolved measurements and computational modeling. Our findings reveal that the light scattering from *C. elegans* arises from two primary sources: volume scattering within the animal body and surface scattering at the interfaces between the animal, air, and the moist substrate. These two types of scattering exhibit distinct angular and spatial profiles and contribute differently to the overall scattering. Surface scattering is more prominent at small and large angles, while volume scattering dominates at intermediate angles (Fig. 2). Volume

371 scattering is highest at the central region of the animal (Fig. 3) and helps resolve internal
372 anatomical structures (Fig. 4). On the other hand, surface scattering enhances the animal's
373 boundaries (Fig. 3), which may aid animal detection and tracking but obscure internal features
374 (Fig. 4). The interplay between the volume and surface scattering suggests that the optimal
375 imaging configuration should be tailored to the specific applications, for example, behavioral
376 tracking versus anatomical visualization.

377 We found that the image contrast is highly sensitive to multiple parameters, including the
378 illumination angle, wavelength, and the type of imaging substrates. These findings inform a set
379 of imaging parameters that enhance image contrast. The simple strategy we provided here does
380 not require specialized optics and labels, and therefore it is readily adaptable to many systems,
381 for example, microscopy [17, 47-50], high-throughput screening setups [10, 18, 19, 51, 52],
382 microfluidic chambers [41, 53, 54], and automation systems [12, 52, 55, 56].

383 Together, this study provides a biophysical understanding for the light–tissue interactions
384 in multiple-scattering organisms and offers physically informed strategies for optimizing the
385 image quality in a wide range of imaging systems. Our findings hold immediate value for
386 researchers using *C. elegans* as a model system, and broader relevance for biological imaging
387 across disciplines, such as genetics, neuroscience, and pharmacology.

388 It is important to acknowledge the limitations of our work. First, some sources of error
389 may affect the accuracy of the scattering function measurements. For example, the imperfect
390 alignment of the components to the optical axis would also contribute to the discrepancy in the
391 measurements of the angle. The LEDs, the FOV of the camera, and the iris of the lens have
392 non-zero sizes, such that the scattered lights we collected are from a finite range of angles.
393 Therefore, in order to minimize the angular uncertainty, we selected lights for particular angles
394 by intentionally setting the numerical aperture of the lens to be low (F-number f/16, NA ≈ 0.031),
395 with an acceptable cost of lower spatial resolution of the images (Fig. 1B, Fig. 3A and C).

There are a few factors that may affect the agreement of our computational model to the experimental data. First, the animal is modeled as a simple cylinder, where the geometry of head and tail and the bending of the body are not captured. Second, optical absorption from the animal is not modeled. Third, we did not model the scattering due to the substrate or bacteria, causing the background noise underestimated in the detected signal. Next, the optical simulation is based on geometric ray tracing where the wave properties of the light, such as diffraction, interference, and polarization, are not modeled.

This study focuses on a single developmental stage (day-1 adult) of a specific *C. elegans* strain (N2). Variations in body morphology, internal structures, or cuticle properties across life stages or genetic backgrounds may alter light scattering patterns [17]. Future work could explore how scattering profiles change across developmental stages and in genetic mutants with altered anatomy.

The calculation of the scattering function and image contrast is on an individual-animal basis, which may neglect the variability between different organs and tissues. For example, pharyngeal muscles are less scattering compared to embryos or intestine (Fig. 4F). Future work will investigate the scattering profiles for different anatomical structures.

We expect the mechanisms of light scattering we identified here to have better explanatory power for transparent, absorption-minimal biological samples, such as other nematodes [57], fruit fly larvae [58], zebrafish larvae [59], and human organoids [60].

Materials and methods

Imaging system

Our imaging system contains a LED ring comprised of 36 RGB LEDs (Qasim, 95 mm diameter), a 3D-printed culture plate holder, a camera lens (Nikon Micro-NIKKOR, effective focal length 105 mm, set to f/16, with C-mount adapter) and a CMOS camera (Imaging Source, DMK 33GP031) (Fig. 1A). All optical elements are mounted to a 1.5" diameter, vertically oriented post (Thorlabs P14) through post mounting clamps (Thorlabs C1511) and they are aligned to be centered on a common optical axis. The distance between the lens and the plate was 400 mm. The illumination angle θ can be varied by translating the LED ring along the optical axis. The LED ring can be mounted below the agar plate to provide angles <90° or above the plate to provide angles between 90° and 180°. Some angles near 0°, 90°, and 180° are unavailable due to constraints of the optical mounts. The LED array is programmable to emit red, green, or blue light. We measured the peak wavelengths of the LEDs using a fiber optic coupled spectrometer (Ocean Optics FLAME-S-XR1) to be 629, 516, and 447 nm. The spectral widths were approximately 16, 26, and 14 nm (FWHM), respectively.

Measurement of scattering functions

The angle-resolved scattering function $p(\theta)$ describes the probability of a photon scattering into a unit solid angle oriented at an angle θ relative to its original trajectory [35, 36]. Here we calculated $p(\theta)$ via the expression (Eq. 1)

$$p(\theta) = \frac{P_{cam}(\theta)}{P_{in}(\theta) \cdot \Omega}$$

where $P_{cam}(\theta)$ is the optical power received by the camera over the region of interest (ROI), $P_{in}(\theta)$ the total optical power incident on the object, and Ω the solid angle collected by the camera lens. We measured incident irradiance using an optical power meter (Coherent FieldMate Laser Power Meter with OP-2 VIS sensor). To calculate $P_{cam}(\theta)$, we used the expression (Eq. 2)

$$P_{cam}(\theta) = \frac{PV(\theta) \cdot A_{roi}}{k \cdot T_{exp}}$$

where A_{roi} is the area of the ROI, T_{exp} the exposure time, and k is the conversion coefficient from irradiance to pixel value. The measured k values for our camera in response to red, green, and blue light are 3.0, 3.3, and 3.5 × 10^5 $ADU \cdot mm^2 \cdot s^{-1} \cdot \mu W^{-1}$ respectively, where ADU is an analog-to-digital unit.

Calculation of the contrast index

We defined the contrast index (CI) for an animal against its background as (Eq. 3)

$$CI = \frac{\overline{PV_w} - \overline{PV_{bg}}}{\overline{PV_w} + \overline{PV_{bg}}}$$

where $\overline{PV_w}$ and $\overline{PV_{bg}}$ are the average pixel values inside the contour of the worm and the background. The contours of the animal were labeled using ImageJ (version 1.54g). The ROI for its background was chosen as a 1.1 mm x 1.1 mm rectangular region adjacent to the animal.

Since the scattering function $p(\theta)$ is proportional to the pixel values $PV(\theta)$ (Eq. 1 and 2), CI can be also expressed as (Eq. 4)

$$CI(\theta) = \frac{\overline{p(\theta)_w} - \overline{p(\theta)_{bg}}}{\overline{p(\theta)_w} + \overline{p(\theta)_{bg}}}$$

Computational modeling

We conducted simulations using Ansys Zemax OpticStudio 2024 R2 optical design and analysis software in non-sequential mode. First, we constructed 3-dimensional models representing *C. elegans* on the culture substrate in the scenarios of non-index matching and index matching (Fig. 2A and B). The simulated animal is illuminated by 36 collimated light sources equally spaced in the azimuthal direction and with polar angle of θ relative to the optical axis of the camera lens, which is modeled as a paraxial lens (f = 105 mm) with an iris (6.56 mm diameter) positioned 400 mm from the animal. The lens forms an image at an image distance of 142.37 mm on the other side. The image is captured by an incoherent irradiance detector. For each angle tested we performed 10 trials of ray tracing, with each trial containing 2×10^8 analyzed rays. We recorded an irradiance map after each trial. Next, we calculated the scattering function $p(\theta)$ based on Eq. 1.

To model the volume scattering, we set the scattering within the simulated animal to follow the Henyey-Greenstein phase function [28] (Fig. 2A and B). The two parameters, the anisotropy factor (g) and mean free path (MFP), were chosen by minimizing the mean squared error between the simulated scattering function and the experimental observations in the index-matched scenario (Fig. 2B and E). The optimized value for the anisotropy parameter was g = 0.83 and the mean free path was MFP = 12 μm.

After obtaining the optimized values for g and MFP, we simulated the complete scattering from the animal using the non-index matched model (Fig. 2A). We optimized the surface scattering by adjusting the shape of the capillary film such that the mean squared error between the simulated scattering function and the experimental data was minimized (Fig. 2E and Fig. S2).

Edge-to-middle contrast index (EMCI)

To calculate the EMCI for the scattering profile across the animal (Fig. 3A-D), we first symmetrically divided the distribution into three portions (Fig. 3B), including the first edge portion (42 μm length), the middle portion (84 μm length), and the second edge portion (42 μm length). Next, we calculated the average value of the scattering function for both edge portions $\overline{p(\theta)_e}$ and for the middle portion $\overline{p(\theta)_m}$. We then calculated EMCI as (Eq. 5)

$$EMCI(\theta) = \frac{\overline{p(\theta)_e} - \overline{p(\theta)_m}}{\overline{p(\theta)_e} + \overline{p(\theta)_m}}$$

Bright field and dark field microscopy

The bright field microscopy images of *C. elegans* (Fig. 4B and C) were obtained using an objective lens (NA = 0.3, Leica 1× planapochromat) on a stereo microscope (Leica M165 FC). The angular range of illuminations was controlled by adjusting the aperture size of the illumination condenser.

The dark field microscopy images of *C. elegans* (Fig. 4E-H) were obtained using an objective lens (NA = 0.14, f = 40 mm, Mitutoyo 5X Plan Apochromat) together with a tube lens (f = 100 mm, Thorlabs TTL100-A) in a custom-built infinity-corrected microscope. Similar to Fig. 1A, the illumination angle is controlled by positioning an LED ring concentric with the optical axis at different distances to the animal.

Preparation of imaging substrates

To prepare different culture substrates used for comparison of image contrast (Fig. 5), we dissolve powders of agar, gelatin, and gellan gum in nematode growth medium (NGM) liquid at 100 ºC and wait until they solidify at room temperature. The concentration of the agar was set to 17 g/L according to the standard protocol [61]. In order to obtain gelatin and gellan gum substrates suitable for maintaining *C. elegans*, we adjusted their concentrations such that the resultant substrates have comparable mechanical strengths as the standard 1.7% agar plate. We measured their mechanical strengths by a puncture test, where the minimum forces for an indenter (active area 19 mm^2) causing fractures on the substrate were recorded by a precision balance (Mettler Toledo MS1602S). After these tests we set the concentration of gelatin to be 10.1% (average strength 79.9 ± 6.7 kPa, mean ± SD, N = 10 plates) and the gellan gum 1.125% (average strength 79.9 ± 5.7 kPa, N = 10), such that their mechanical strengths are comparable to the standard 1.7% agar plates (average strength 85.1 ± 9.3 kPa, N = 10).

Preparation of *C. elegans*

The N2 *C. elegans* strain used in this study was cultivated at 20°C on NGM plates with OP50 bacteria using standard methods [61]. We performed timed egg laying assays within a 4-hour window for synchronizing the ages of the animals. We used day 1 adults for all the experiments. All experiments were performed at room temperature (approximately 20 ºC).

Data, materials, and software availability

The raw data for this paper is available in *SI Appendix*, Dataset S1. The design file for constructing the 3D models is available in *SI Appendix*, Design File S1. The source file for the optical simulation is available in *SI Appendix*, Software S1. The source code for the data analysis is available in *SI Appendix*, Software S2.

Acknowledgments

This research was supported by The National Institutes of Health (R01DA056358). The *C. elegans* strain was provided by the *Caenorhabditis* Genetics Center, funded by the NIH Office of Research Infrastructure Programs (P40 OD010440). We thank Animesh Biswas and Hongfei Ji for helpful discussions and suggestions.

References

1. Brenner, S., *The genetics of Caenorhabditis elegans.* Genetics, 1974. **77**(1): p. 71-94.
2. Corsi, A.K., B. Wightman, and M. Chalfie, *A transparent window into biology: a primer on Caenorhabditis elegans.* Genetics, 2015. **200**(2): p. 387-407.
3. Cook, S.J., et al., *Whole-animal connectomes of both Caenorhabditis elegans sexes.* Nature, 2019. **571**(7763): p. 63-71.
4. Yemini, E., et al., *A database of Caenorhabditis elegans behavioral phenotypes.* Nature methods, 2013. **10**(9): p. 877-879.

5. Nguyen, J.P., et al., *Whole-brain calcium imaging with cellular resolution in freely behaving Caenorhabditis elegans.* Proceedings of the National Academy of Sciences, 2016. **113**(8): p. E1074-E1081.

6. Venkatachalam, V., et al., *Pan-neuronal imaging in roaming Caenorhabditis elegans.* Proceedings of the National Academy of Sciences, 2016. **113**(8): p. E1082-E1088.

7. Randi, F., et al., *Neural signal propagation atlas of Caenorhabditis elegans.* Nature, 2023. **623**(7986): p. 406-414.

8. Javer, A., et al., *An open-source platform for analyzing and sharing worm-behavior data.* Nature methods, 2018. **15**(9): p. 645-646.

9. Fryer, E., et al., *A high-throughput behavioral screening platform for measuring chemotaxis by C. elegans.* PLoS Biology, 2024. **22**(6): p. e3002672.

10. Barlow, I.L., et al., *Megapixel camera arrays enable high-resolution animal tracking in multiwell plates.* Communications biology, 2022. **5**(1): p. 253.

11. Crane, M.M., et al., *Autonomous screening of C. elegans identifies genes implicated in synaptogenesis.* Nature methods, 2012. **9**(10): p. 977-980.

12. Li, Z., et al., *A robotic system for automated genetic manipulation and analysis of Caenorhabditis elegans.* PNAS nexus, 2023. **2**(7): p. pgad197.

13. Pan, P., et al., *Robotic microinjection enables large-scale transgenic studies of Caenorhabditis elegans.* Nature Communications, 2024. **15**(1): p. 8848.

14. Rohde, C.B., et al., *Microfluidic system for on-chip high-throughput whole-animal sorting and screening at subcellular resolution.* Proceedings of the National Academy of Sciences, 2007. **104**(35): p. 13891-13895.

15. Le, K.N., et al., *An automated platform to monitor long-term behavior and healthspan in Caenorhabditis elegans under precise environmental control.* Communications biology, 2020. **3**(1): p. 297.

16. Sohrabi, S., et al., *High-throughput behavioral screen in C. elegans reveals Parkinson's disease drug candidates.* Communications Biology, 2021. **4**(1): p. 203.
17. Fouad, A.D., et al., *Quantitative assessment of fat levels in Caenorhabditis elegans using dark field microscopy.* G3: Genes, Genomes, Genetics, 2017. **7**(6): p. 1811-1818.
18. Churgin, M.A., et al., *Longitudinal imaging of Caenorhabditis elegans in a microfabricated device reveals variation in behavioral decline during aging.* Elife, 2017. **6**: p. e26652.
19. Ji, H., D. Chen, and C. Fang-Yen, *Automated multimodal imaging of Caenorhabditis elegans behavior in multi-well plates.* Genetics, 2024. **228**(4): p. iyae158.
20. Sulston, J.E. and H.R. Horvitz, *Post-embryonic cell lineages of the nematode, Caenorhabditis elegans.* Developmental biology, 1977. **56**(1): p. 110-156.
21. Husson, S.J., et al., *Keeping track of worm trackers.* WormBook: The Online Review of C. elegans Biology [Internet], 2018.
22. Wang, L.V. and H.-i. Wu, *Biomedical optics: principles and imaging*. 2007: John Wiley & Sons.
23. Mertz, J., *Introduction to optical microscopy*. 2019: Cambridge University Press.
24. McDonald, J., *Optical microscopy*, in *Microelectronics Failure Analysis: Desk Reference*. 2019, ASM International. p. 42-61.
25. Wax, A. and V. Backman, *Biomedical Applications of Light Scattering (McGraw-Hill Professional).* 2009.
26. Mie, G., *Beiträge zur Optik trüber Medien, speziell kolloidaler Metallösungen.* Annalen der physik, 1908. **330**(3): p. 377-445.
27. Keener, J.D., et al., *Application of Mie theory to determine the structure of spheroidal scatterers in biological materials.* Optics letters, 2007. **32**(10): p. 1326-1328.
28. Henyey, L.G. and J.L. Greenstein, *Diffuse radiation in the galaxy.* Astrophysical Journal, vol. 93, p. 70-83 (1941). 1941. **93**: p. 70-83.

29. Binzoni, T., et al., *The use of the Henyey–Greenstein phase function in Monte Carlo simulations in biomedical optics.* Physics in Medicine & Biology, 2006. **51**(17): p. N313.

30. Jacques, S.L., C. Alter, and S.A. Prahl, *Angular dependence of HeNe laser light scattering by human dermis.* Lasers Life Sci, 1987. **1**(4): p. 309-333.

31. Popp, A.K., et al., *Microscopic origin of light scattering in tissue.* Applied optics, 2003. **42**(16): p. 2871-2880.

32. Ruf, D., et al. *Differentiation of biological tissue based on angle-resolved scattering distribution using fiber-coupled single-mode light source with spectrally controllable emission characteristics*. in *Optical Methods for Inspection, Characterization, and Imaging of Biomaterials VI*. 2023. SPIE.

33. Bolt, R.A., J.S. Kanger, and F.F. de Mul. *Angular dependence of light scattering by biological tissue*. in *Biomedical Sensors, Fibers, and Optical Delivery Systems*. 1999. SPIE.

34. Cross, D.A. and P. Latimer, *Angular dependence of scattering from Escherichia coli cells.* Applied optics, 1972. **11**(5): p. 1225-1228.

35. Hulst, H.C. and H.C. van de Hulst, *Light scattering by small particles*. 1981: Courier Corporation.

36. Van de Hulst, H., *Multiple light scattering.* New York: Academic, 1981. **1**.

37. Jacques, S.L., *Optical properties of biological tissues: a review.* Physics in Medicine & Biology, 2013. **58**(11): p. R37.

38. Cheong, W.-F., S.A. Prahl, and A.J. Welch, *A review of the optical properties of biological tissues.* IEEE journal of quantum electronics, 2002. **26**(12): p. 2166-2185.

39. Khan, R., et al., *Refractive index of biological tissues: Review, measurement techniques, and applications.* Photodiagnosis and photodynamic therapy, 2021. **33**: p. 102192.

40. Choi, W., et al., *Tomographic phase microscopy.* Nature methods, 2007. **4**(9): p. 717-719.

41. Ji, H., et al., *A proprioceptive feedback circuit drives Caenorhabditis elegans locomotor adaptation through dopamine signaling.* Proceedings of the National Academy of Sciences, 2023. **120**(20): p. e2219341120.

42. Ji, H., et al., *Phase response analyses support a relaxation oscillator model of locomotor rhythm generation in Caenorhabditis elegans.* Elife, 2021. **10**: p. e69905.

43. Rabets, Y., et al., *Direct measurements of drag forces in C. elegans crawling locomotion.* Biophysical journal, 2014. **107**(8): p. 1980-1987.

44. Boutry, G.-A., *Augustin Fresnel: his time, life and work, 1788-1827.* Science Progress (1933-), 1948. **36**(144): p. 587-604.

45. Brinke, M., P. Heininger, and W. Traunspurger, *A semi-fluid gellan gum medium improves nematode toxicity testing.* Ecotoxicology and Environmental Safety, 2011. **74**(7): p. 1824-1831.

46. Kwon, N., et al., *Dissection of C. elegans behavioral genetics in 3-D environments.* Scientific reports, 2015. **5**(1): p. 9564.

47. Shi, R., et al., *Asymmetrical Illumination Enables Lipid Droplets Segmentation in Caenorhabditis elegans Using Epi-Illumination Dark Field Microscopy.* Frontiers in Physics, 2022. **10**: p. 894797.

48. Shi, R., et al., *Epi-illumination dark-field microscopy enables direct visualization of unlabeled small organisms with high spatial and temporal resolution.* Journal of Biophotonics, 2022. **15**(1): p. e202100185.

49. Nigamatzyanova, L. and R. Fakhrullin, *Dark-field hyperspectral microscopy for label-free microplastics and nanoplastics detection and identification in vivo: A Caenorhabditis elegans study.* Environmental Pollution, 2021. **271**: p. 116337.

641 50. Zhang, N., et al., *An automatic recognition method of nematode survival rate based on*
642 *bright field and dark field experimental images.* Technology and Health Care, 2023.
643 **31**(1_suppl): p. 199-208.
644 51. Churgin, M.A., et al., *Quantitative imaging of sleep behavior in Caenorhabditis elegans*
645 *and larval Drosophila melanogaster.* Nature Protocols, 2019. **14**(5): p. 1455-1488.
646 52. Fouad, A.D., et al., *High-throughput imaging of Caenorhabditis elegans aging using*
647 *collective activity monitoring.* bioRxiv, 2021: p. 2021.10. 18.464905.
648 53. San-Miguel, A. and H. Lu, *Microfluidics as a tool for C. elegans research.* WormBook:
649 The Online Review of C. elegans Biology [Internet], 2018.
650 54. Aubry, G. and H. Lu, *A perspective on optical developments in microfluidic platforms for*
651 *Caenorhabditis elegans research.* Biomicrofluidics, 2014. **8**(1).
652 55. Stelzer, C.P. and D. Groffman, *Wellcounter: Automated high‐throughput phenotyping for*
653 *aquatic microinvertebrates.* Methods in Ecology and Evolution, 2025. **16**(5): p. 958-971.
654 56. Stepanov, I., et al., *Low-cost robotic manipulation of live microtissues for cancer drug*
655 *testing.* Science Advances, 2025. **11**(20): p. eads1631.
656 57. Nigon, V.M. and M.-A. Félix, *History of research on C. elegans and other free-living*
657 *nematodes as model organisms.* WormBook: The Online Review of C. elegans Biology
658 [Internet], 2018.
659 58. Yamaguchi, M. and H. Yoshida, *Drosophila as a model organism.* Drosophila models for
660 human diseases, 2018: p. 1-10.
661 59. Basnet, R.M., et al., *Zebrafish larvae as a behavioral model in neuropharmacology.*
662 Biomedicines, 2019. **7**(1): p. 23.
663 60. Kim, J., B.-K. Koo, and J.A. Knoblich, *Human organoids: model systems for human*
664 *biology and medicine.* Nature reviews Molecular cell biology, 2020. **21**(10): p. 571-584.

61. Stiernagle, T., *Maintenance of C. elegans.* WormBook: The online review of C. elegans biology [Internet], 2006.

Supplementary material

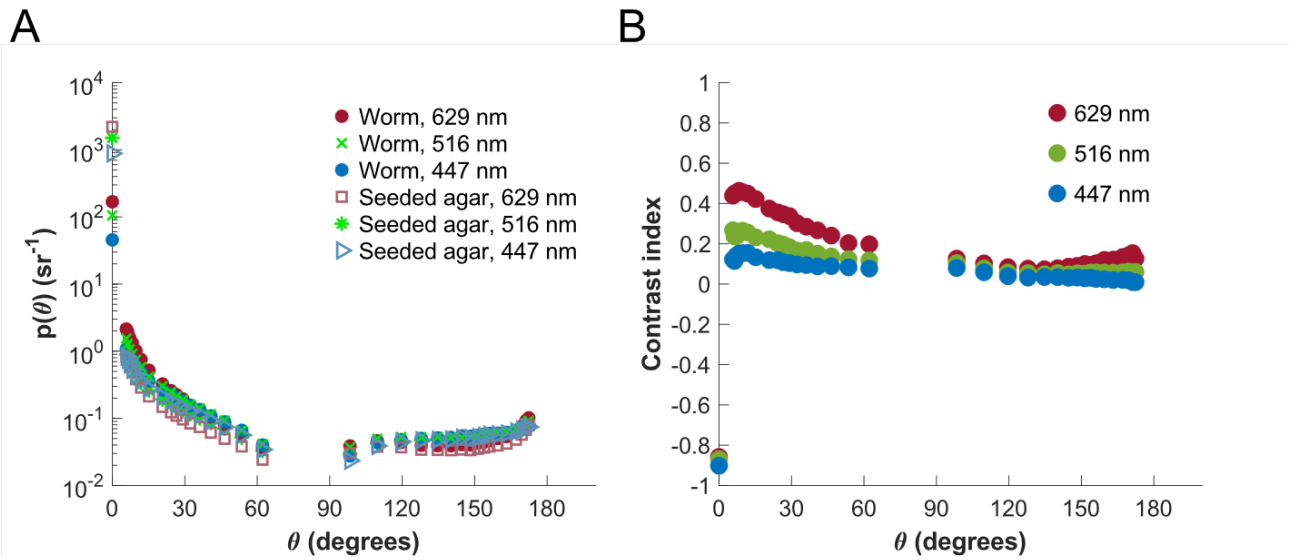

Fig. S1. (A) Angle-resolved scattering functions for *C. elegans* and seeded agar for the index matched scenario under red, green, and blue illumination. (B) Image contrast index for *C. elegans* on seeded agar as a function of illumination angle and wavelength for the index matched case.

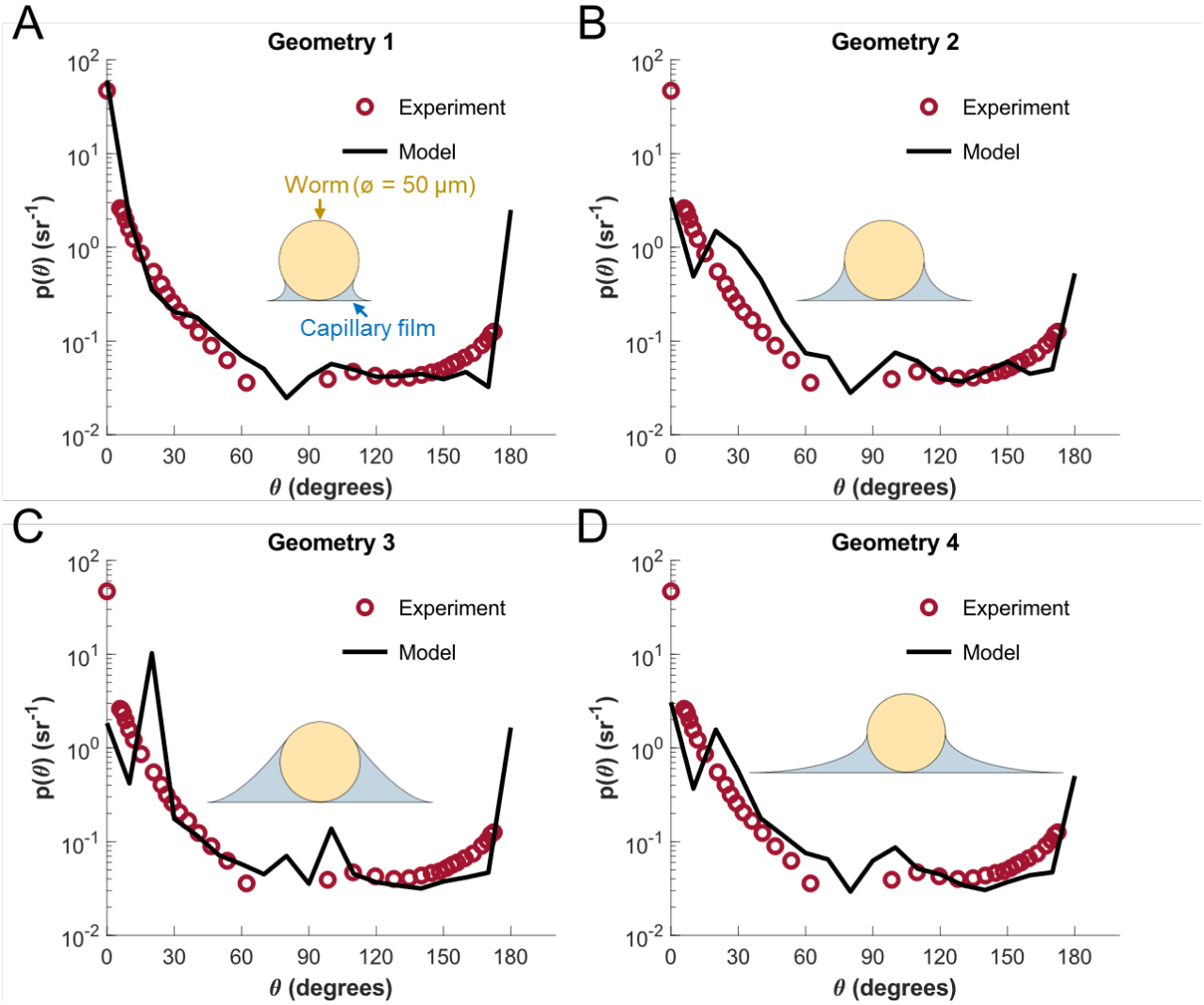

Fig. S2. Scattering functions of *C. elegans* obtained from the experiment (on seeded agar under 629-nm illumination) and the computational models with different geometries of capillary water film. Insets: the cross section of the simulated animal and capillary water film.

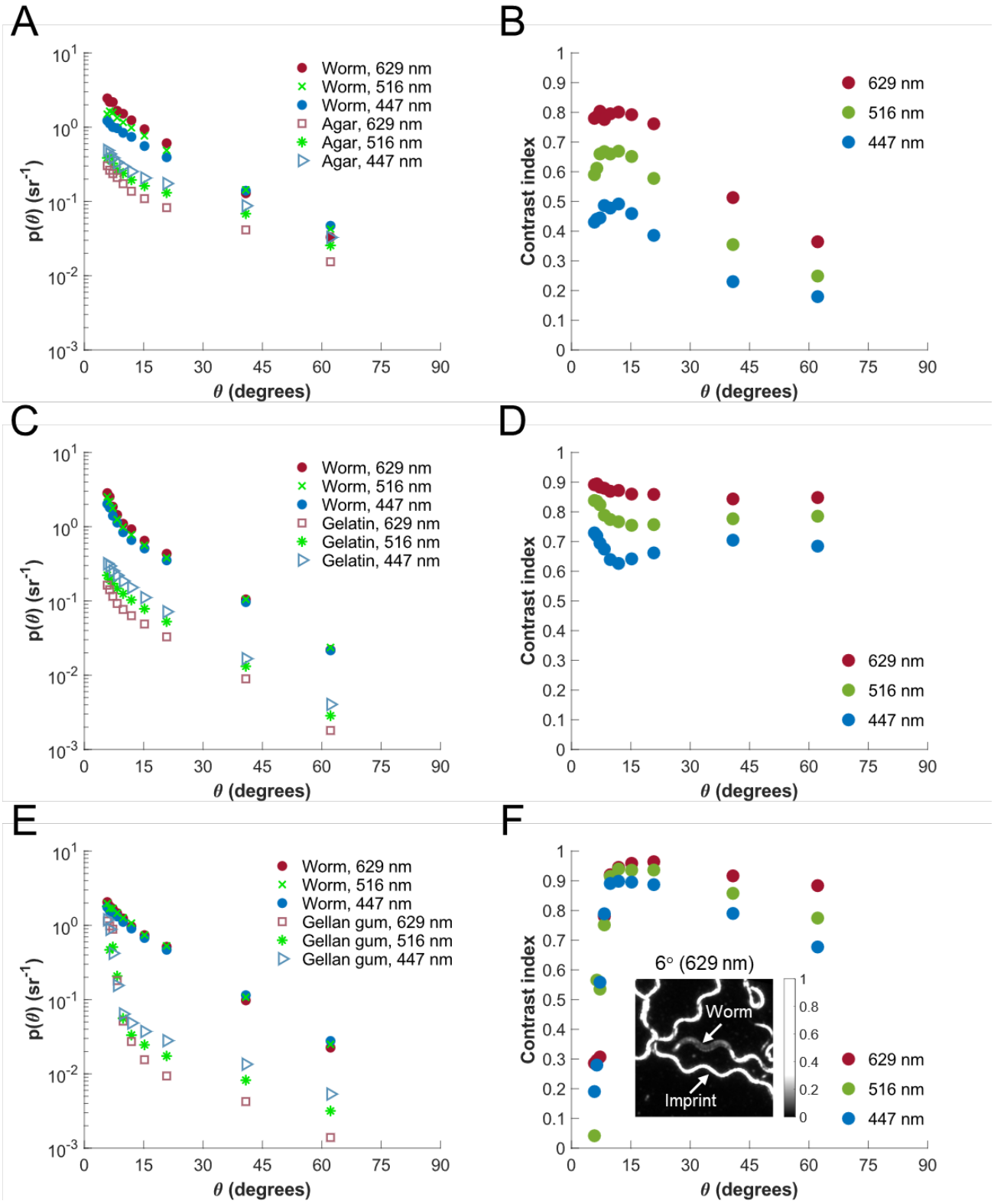
A
B
C
D
E
F
Worm, 629 nm
Worm, 516 nm
Worm, 447 nm
Agar, 629 nm
Agar, 516 nm
Agar, 447 nm
Gelatin, 629 nm
Gelatin, 516 nm
Gelatin, 447 nm
Gellan gum, 629 nm
Gellan gum, 516 nm
Gellan gum, 447 nm
p(θ) (sr-1)
Contrast index
θ (degrees)
629 nm
516 nm
447 nm
6° (629 nm)
Worm
Imprint

682

683 **Fig. S3.** Angle-resolved, wavelength-dependent scattering functions and image contrast for *C.*
684 *elegans* on unseeded media made with (A and B) agar, (C and D) gelatin, and (E and F) gellan
685 gum. Inset of (F): a representative image of *C. elegans* and its imprints on unseeded gellan gum
686 under a red illumination applied at 6º (FOV: 2.22 × 2.22 mm).

687

Dataset S1 (separate file). Raw data for the plots presented in this paper.

Design File S1 (separate file). Design files (in STEP format) for the 3D models representing *C. elegans* and its surroundings.

Software S1 (separate file). Source files (in ZMX and ZPL format) for conducting the optical simulations.

Software S2 (separate file). Source MATLAB scripts for the data analysis performed in this study.